

This is the accepted manuscript made available via CHORUS. The article has been published as:

First-principles study of the atomic and electronic structures of misfit-layered calcium cobaltite $(\text{Ca}_{\{2\}}\text{CoO}_{\{3\}})(\text{CoO}_{\{2\}})_{\{1.62\}}$ using rational approximants

Alejandro Rébola, Robert Klie, Peter Zapol, and Serdar Ögüt

Phys. Rev. B **85**, 155132 — Published 19 April 2012

DOI: [10.1103/PhysRevB.85.155132](https://doi.org/10.1103/PhysRevB.85.155132)

First principles study of the atomic and electronic structures of misfit-layered calcium cobaltite $(\text{Ca}_2\text{CoO}_3)(\text{CoO}_2)_{1.62}$ using rational approximants

Alejandro Rébola,^{1,2} Robert Klie,¹ Peter Zapol,² and Serdar Ögüt¹

¹*Department of Physics, University of Illinois at Chicago, Chicago, IL 60607 USA*

²*Materials Science Division, Argonne National Laboratory, Argonne, IL 60439 USA*

(Dated: March 26, 2012)

The atomic and electronic structures of the misfit-layered thermoelectric oxide material, $\text{Ca}_3\text{Co}_4\text{O}_9$, are investigated using detailed first principles computations performed within the framework of density functional theory (DFT) and its DFT+U extension to account for electron correlations. The structure of $\text{Ca}_3\text{Co}_4\text{O}_9$, composed of two incommensurate subsystems, a distorted rocksalt-type Ca_2CoO_3 layer sandwiched between hexagonal CoO_2 layers, is modeled by means of Fibonacci rational approximants with systematically increasing unit cells. We show that good agreement with photoemission and transport experiments can be obtained regarding the contribution of the two subsystems to states near the Fermi level, when electron correlations are taken into account with a Hubbard U . The size of the rational approximant plays a secondary role in the analysis; the relatively “small” structure of composition $(\text{Ca}_2\text{CoO}_3)_6(\text{CoO}_2)_{10}$ represents a good model for investigating the atomic and electronic properties of $\text{Ca}_3\text{Co}_4\text{O}_9$. Within the DFT+U formalism, the metallic conductivity of $\text{Ca}_3\text{Co}_4\text{O}_9$ is shown to result from itinerant holes in the hexagonal CoO_2 layers, in which the Co atoms are predicted to have a mixed valence of Co^{4+} with $\sim 30\%$ concentration and Co^{3+} with $\sim 70\%$ concentration, both in low-spin configurations. In most cases, the resulting electronic structures show very good agreement with available data from transport and magnetic measurements.

PACS numbers: 71.20.-b, 61.44.Fw, 71.15.Mb, 72.15.Jf

I. INTRODUCTION

Transition metal oxides have been the focus of many experimental, theoretical, and computational studies, as they exhibit a wide range of functional properties including colossal magneto-resistance, two-dimensional electron gas, (multi)-ferroism, and superconductivity, to name a few. It was suggested a while ago that bringing two transition metal oxides with different properties in close proximity with each other might result in the emergence of novel and exciting phases not seen in either bulk structure.^{1,2} For example, one such novel phase stabilized by combining an insulating oxide with a distorted rocksalt structure and a Mott-insulator oxide can exhibit high efficiency thermoelectric transport.³ Such a combination would not only satisfy the subsystem approach, where one subsystem fulfills the role of the “electron crystal” while the other acts as a “phonon glass”, but the interfacial effects can also be expected to lead to a significant enhancement of the electron transport, not seen in pure bulk phases. Incommensurately-layered cobalt oxides,^{4–9} in particular $\text{Ca}_3\text{Co}_4\text{O}_9$, (CCO), also reported as $(\text{Ca}_2\text{CoO}_3)(\text{CoO}_2)_{1.62}$, represent one such system, where the close proximity between the layers of rocksalt (RS) Ca_2CoO_3 and hexagonal CoO_2 results in a high in-plane Seebeck coefficient, S , and more importantly, a high thermoelectric figure of merit, ZT , at elevated temperatures. Furthermore, CCO stands out as the only layered cobalt oxide system containing one cation with nominally different oxidation states in both subsystems, namely Co^{2+} in the RS layers and Co^{4+} in the hexagonal CoO_2 layers. This makes CCO an ideal system for studying effects such as charge transfer or orbital ordering both experimentally and theoretically.

Since the pioneering experimental study of Masset *et al.*¹⁰ who reported the structural model of CCO along with its temperature-dependent magnetic and transport properties, there have been several other experimental studies about the structural, electronic, magnetic, and thermoelectric properties of CCO in its pristine^{10–26} as well as doped forms with various types of cation substitutions.^{27–34} The structure of CCO was reported to be monoclinic with two misfit-layered subsystems, a distorted RS-type Ca_2CoO_3 layer sandwiched between two CdI₂-type CoO_2 layers along the c -direction. Both subsystems share the same a and c lattice parameters, but they are incommensurate along the b direction. Among the experimental studies to date, of particular importance is the study by Takeuchi *et al.*¹⁴ who investigated the electronic structure of CCO using high resolution photoemission spectroscopy and demonstrated that the large thermoelectric power of CCO could be well accounted for with the Boltzmann-type metallic electrical conduction. The authors also argued that the metallic conduction in CCO was due to the hexagonal CoO_2 layer, not the RS subsystem. This suggestion was also supported by resistivity and Hall measurements of Eng *et al.*¹⁹ who argued that the transport properties of CCO were essentially governed by itinerant holes in the CoO_2 layers.

In spite of significant experimental effort to characterize and improve its thermoelectric properties, there have been few theoretical or computational studies on CCO.^{24,35,36} To some extent, this is due to the computational challenge posed by modeling an incommensurate crystal. Asahi *et al.* carried out the first *ab initio* calculations on CCO within the framework of density functional theory (DFT): Using an approximate unit cell of composition $(\text{Ca}_2\text{CoO}_3)_4(\text{CoO}_2)_6$, they performed a comprehensive study of the structural, electronic, magnetic, and thermoelectric properties of CCO.³⁵ While the computations of Asahi *et al.* provided a great deal of information at the microscopic level to aid in the interpretation of experiments and accounted for some of the experimental observations, their finding that only the RS subsystem contributes to the density of states at the Fermi level was later shown to be in contradiction with the interpretations of Takeuchi *et al.* from their photoemission experiments.

In the present study, we report results from first principles calculations performed within a DFT framework on CCO using structural models with systematically increasing unit cell sizes. As mentioned before, the composition of CCO can be described relatively well as $(\text{Ca}_2\text{CoO}_3)(\text{CoO}_2)_{1.62}$ which means that the composition ratio of the two subsystems is very close to the golden mean $\tau = (1 + \sqrt{5})/2 \approx 1.618$, which commonly appears in the study of quasicrystals.³⁷ Taking into account that τ is the limit of the sequence of the ratios of consecutive Fibonacci numbers $F(n+1)/F(n) = 2, 3/2, 5/3, 8/5, 13/8, \dots \rightarrow \tau$, we model the incommensurate structure of CCO by using supercells with composition $(\text{Ca}_2\text{CoO}_3)_{2F(n)}(\text{CoO}_2)_{2F(n+1)}$. Using the same terminology as in the study of quasicrystals,³⁷ we call such supercells “rational approximants” to CCO. In this study, we consider four consecutive approximants of increasing supercell sizes, namely the 3/2, 5/3, 8/5, and 13/8 approximants, the smallest of which is the one considered by Asahi *et al.* For each approximant, we determine the structural and electronic properties using local and gradient-corrected exchange-correlation functionals, as well as using the DFT+U formalism^{38,39} to account for enhanced electron correlations. We show that good agreement with photoemission experiments can be obtained when correlations are taken into account in the RS subsystem, while the size of the approximant plays a secondary role. The rest of the paper is organized as follows. In the next section, we outline the computational methods and parameters used in this study. The results and discussion of our first principles computations for the structural, electronic, magnetic, and thermoelectric properties of various approximants used to model CCO within DFT and DFT+U are presented in Sec. III. We conclude with a brief summary in Sec. IV.

II. COMPUTATIONAL METHODS AND PARAMETERS

Monoclinic unit cells of CCO were constructed for the different rational approximants. The lattice parameters were initially set at the experimental values¹¹ along the periodic directions as $a = 4.83 \text{ \AA}$, $c = 10.84 \text{ \AA}$, and $\beta = 98.13^\circ$. The periodicities of the Ca_2CoO_3 RS and CoO_2 hexagonal subsystems along the b direction are incommensurate with each other. As a result, CCO can be stoichiometrically expressed as $(\text{Ca}_2\text{CoO}_3)_{b_1/b_2}(\text{CoO}_2)_{b_1/b_2}$, where b_1 and b_2 correspond to the periodicities of the RS and CoO_2 subsystems along the incommensurate b direction, respectively. The corresponding experimental values are $b_1^{\text{exp}} = 4.56 \text{ \AA}$ and $b_2^{\text{exp}} = 2.82 \text{ \AA}$, yielding $b_1^{\text{exp}}/b_2^{\text{exp}} \approx 1.62$. In order to build the different rational approximants with composition $(\text{Ca}_2\text{CoO}_3)_{2F(n)}(\text{CoO}_2)_{2F(n+1)}$ we took the initial lattice parameters b of the monoclinic unit cell along the incommensurate direction by an average, such that $2b = F(n)b_1^{\text{exp}} + F(n+1)b_2^{\text{exp}}$. This results in starting periodicities of b_{RS} and b_{CoO_2} for the two subsystems, where $2b_{\text{RS}} = b_1^{\text{exp}} + F(n+1)b_2^{\text{exp}}/F(n)$ and $2b_{\text{CoO}_2} = b_2^{\text{exp}} + F(n)b_1^{\text{exp}}/F(n+1)$. In the present study, we considered four rational approximants for CCO, namely the 3/2, 5/3, 8/5, and 13/8 approximants with 42, 66, 108, and 174 atoms in the unit cell, respectively. The initial lattice parameters b along the incommensurate direction for those approximants are 8.79, 13.89, 22.68, and 36.57 \AA , respectively. Various views of unit cell for the unrelaxed 5/3 approximant are shown in Fig. 1.

The calculations were performed using the projector augmented wave (PAW) method as implemented in VASP.⁴⁰ All internal as well as lattice parameters (a, b, c, β) were allowed to relax in the structural optimizations, where we used a plane wave cutoff of 530 eV and a residual force criterion of 0.02 eV/ \AA . During structural optimizations, we used Monkhorst-Pack (MP) \mathbf{k} -point grids of $6 \times 3 \times 3$, $6 \times 2 \times 3$, $6 \times 2 \times 3$, and $4 \times 1 \times 2$ for the 3/2, 5/3, 8/5, and 13/8 approximants, respectively. For the density of states calculations, we used the same cutoff energy and the tetrahedron method with MP grids of $12 \times 6 \times 6$, $12 \times 4 \times 6$, $12 \times 2 \times 6$, and $12 \times 2 \times 6$ for the 3/2, 5/3, 8/5, and 13/8 approximants, respectively. The calculations were performed within the local (spin) density approximation (LDA) using the Ceperley Alder (CA) functional,⁴¹ as well as with the generalized gradient approximation using the Perdew-Burke-Ernzerhof (PBE) functional.⁴² We have carefully examined the dependence of the results on the choice of the exchange-correlation functional, and note that the main conclusions reported in this paper do not have a significant dependence on this choice. Accordingly, unless otherwise noted, all results for the atomic and electronic structures of CCO are reported for the LDA-CA exchange-correlation functional. The calculations were performed for the ferromagnetic spin configuration of the Co atoms. The initial magnetic moments for all Co atoms were set at $1.3 \mu_B$. We tested the dependence of the convergence to the correct ground state on the initial magnetic moment by restarting all computations for the 3/2 and 5/3 approximants with different starting moments of 2.0, 1.5, and $1.0 \mu_B$.

In order to provide a better description of the correlations between the rather localized d electrons of Co, we also performed LDA+U computations for all rational approximants of CCO following Dudarev's approach,⁴³ as implemented in VASP. With $J = 1 \text{ eV}$, we considered values of 3, 5, and 7 eV for the on-site Coulomb repulsion term U . Values near $U = 5 \text{ eV}$ were suggested and successfully used in previous DFT calculations carried out on Na_xCoO_2 and CoO_2 .^{44,45} In addition, we also computed the effective U parameters for Co atoms in the RS and CoO_2 subsystems from first principles using a linear response approach,⁴⁶ as implemented in the Quantum Espresso package.⁴⁷ The results from these computations will be discussed in the next section.

III. RESULTS AND DISCUSSION

A. Structural parameters

Starting with the experimental lattice and internal parameters as described above, full structural optimizations were carried out on all approximants. The results for the relaxed lattice parameters are displayed in Table I. For the a and c lattice parameters, we observe no significant variations as a function of the approximant used. Within LDA, a and c are underestimated by $\sim 1.5\text{--}2\%$ and $\sim 3\%$, respectively. Along the incommensurate direction, on the other hand, the relaxed lattice parameters b_{RS} and b_{CoO_2} are, by construction, expected to show larger variations with respect to the approximant size. This is indeed what we observe in Table I, where b_{RS} and b_{CoO_2} converge somewhat slowly to values near 4.5 and 2.8 \AA , respectively, which are slightly underestimated with respect to experimental values, consistent with the trends observed within LDA. Repeating the calculations with PBE exchange-correlation functional, we find that the lattice parameters are slightly (1–2%) overestimated compared to experimental values, as expected. As shown in Table I for the 3/2 approximant, the agreement with experiment is slightly better with the PBE functional compared to LDA, especially for the c lattice parameter.

Fractional coordinates for the internal parameters computed for all the approximants are shown in Table II along with the experimental values. The agreement with experimental values is quite reasonable (within a few percent), except for the fractional coordinates of Co along the a -axis in the RS subsystem and O1 along the c -axis in the CoO_2 subsystem where the deviations from experiment increase to around 10%. When we repeat the calculations with the

PBE exchange-correlation functional, most of the fractional coordinates get closer to experimental values, however, the coordinate of O2 along the a -axis in the RS subsystem becomes significantly worse, in agreement with Asahi's earlier results.³⁵ Overall, the choice of the exchange-correlation functional does not seem to affect the agreement of the computed internal coordinates with experimental values. We also observe that the internal parameters are not very sensitive to the choice of the approximant, with average deviations staying near 3% and 2% along the a - and c -axes, respectively, for all approximants considered.

The structures were also fully re-optimized within the DFT+U formalism. The resulting lattice parameters for $U = 5$ eV are displayed in Table III. The inclusion of U does not result in a significant change for a and b lattice parameters or the angle β . However, the c lattice constants increases by $\sim 1\%$ within LDA. The inclusion of U within PBE decreases the lattice constants slightly, and generally results in better agreement with experimental values. The fractional coordinates computed with $U = 5$ eV are shown in Table IV. Overall, the PBE and LDA results are observed to be rather close to each other for the fractional coordinates. The agreement with experimental values, on the other hand, is not particularly better compared to $U = 0$ case.

We note that full optimization of the unit cells (for both $U = 0$ and $U \neq 0$) leads to the emergence of interesting structural patterns along the incommensurate b direction as a function of the approximant size. In particular, the RS unit of composition Ca_2CoO_3 forms various n -unit clusters. Using the notation $X \equiv \text{Ca}_2\text{CoO}_3$ for the sake of simplicity and denoting an n -unit Ca_2CoO_3 cluster by X_n , the arrangement of atoms along the b direction can be viewed as $X_n - X_m - \dots$, where each X_n cluster is separated from its neighbors slightly due to the buckling of the O-Co-O chains along the c direction, but still joined with each other along the b direction with Ca-O bonds. As shown in Fig. 2, the relaxation leads to the emergence of a $X_3 - X_1$ structural pattern for the 3/2 approximant composed of one 3-unit and one 1-unit clusters along the b direction. The 5/3 approximant can be viewed as two identical 3-unit clusters, $X_3 - X_3$ joined with each other. The 8/5 approximant can similarly be viewed as a $X_3 - X_2 - X_3 - X_2$ pattern fitting within one b lattice parameter. The most complicated pattern occurs for the 13/8 approximation, composed of various 1-, 2-, 3-, and 4-unit clusters, and is of the form $X_4 - X_2 - X_1 - X_2 - X_4 - X_3$. The particular pattern adopted by a given approximation is related to the incommensurate nature of the CoO_2 and RS subsystems, and depends critically on how the system can minimize the total energy globally within the constraints imposed by the ratio of the Fibonacci numbers. The effects of these structural patterns on the electronic structure of CCO will be discussed toward the end of the next section.

B. Electronic Properties

1. Density of States Analysis

In order to gain insight into the transport properties of CCO we focused on the different contributions to the density of states (DOS) around the Fermi level (E_f) from the two subsystems, RS and CoO_2 . While we performed the DOS analyses for all the approximants considered, in what follows we will first present our results in detail for the 5/3 approximant and later comment on the trends as a function of the approximant. Figure 3 shows spin-polarized total DOS for CCO. Low-energy features in the range of -21 to -16 eV correspond to states that originate from the Ca $3p$ and O $2s$ orbitals, and the features at high energies around 8 eV correspond to the unoccupied Ca $3d$ levels. The states from -8 to 3 eV around E_f are due to strong hybridization among O $2p$ and Co $3d$ orbitals. The contributions to the DOS at E_f are primarily from one of the spin channels (down), as E_f falls in a pseudogap in the spin-up channel. There is a (real) gap in the electronic DOS for the spin-down channel in the vicinity of E_f as well, but that occurs ~ 0.2 eV above E_f . Similar features were observed for the total DOS of the 3/2, 8/5 and 13/8 approximants.

Figure 4 shows the site-projected partial DOS (PDOS) for Co $3d$ orbitals in the RS and CoO_2 subsystems; in each plot the PDOS are displayed after averaging over all Co atoms in the particular subsystem. The Co $3d$ states in the CoO_2 subsystem have a small, but finite, contribution to the DOS at E_f only in the spin-down channel, where E_f lies ~ 0.3 eV below the gap. The Co $3d$ states in the RS subsystem, on the other hand, contribute to the DOS at E_f in both spin channels. Comparing Figs. 3 and 4, one can see quite well that in the spin-up channel the DOS in the immediate vicinity of E_f is controlled primarily by states originating from Co $3d$ orbitals in the RS system, while both subsystems contribute to DOS near E_f in the spin-down channel. The PDOS projections into magnetic angular momentum (m) resolved Co d orbitals in each subsystem are shown in Fig. 5 and 6 for the CoO_2 and RS subsystems, respectively. We observe that t_{2g} bands of the CoO_2 system are fully occupied in the spin-up channel. In the spin-down channel, they are mostly, but not fully occupied, contributing to the finite DOS at E_f . The e_g bands of the CoO_2 system, on the other hand, are fully unoccupied lying ~ 1.2 eV above E_f (Fig. 5). In the RS subsystem, all three $t_{2g,\uparrow}$ bands are occupied while the $e_{g,\uparrow}$ bands are partially occupied. In the minority-spin channel, one of the t_{2g} bands, $d_{xy,\downarrow}$, is noticeably lower in energy and is almost fully occupied, while the other two are partially occupied. The $e_{g,\downarrow}$ bands of the RS system are mostly unoccupied (Fig. 6).

While there are some differences between our results for the RS subsystem and previous computations of Asahi *et al.*, the differences are mostly minor and the agreement between the two sets of DFT calculations is reasonably good for the RS subsystem. The main difference between our results and those of Asahi *et al.*, which has implications for transport properties of CCO, occurs in the CoO₂ subsystem: Namely, while we find that 3*d* orbitals of the CoO₂ system contribute to the DOS at E_f (Fig. 4 upper panel or the spin-down panel of Fig. 5), Asahi *et al.* do not find any contribution from this subsystem to the DOS at E_f which falls in the crystal-field gap of the CoO₂ 3*d* states setting these Co atoms to be in the low-spin Co³⁺ ($S = 0$) state. In contrast, our results suggest that a fraction of the Co atoms in the CoO₂ subsystem are in the Co⁴⁺ state due to the partially occupied $t_{2g,\downarrow}$ bands that cross E_f . The finding of no contribution to DOS from the CoO₂ system, therefore, led Asahi *et al.* to conclude that the conductivity of CCO must be due to the RS subsystem while the CoO₂ subsystem would be acting merely as a charge reservoir. This reasonable conclusion is, however, contradicted by resonant photoemission spectroscopy experiments carried out by Takeuchi *et al.*¹⁴ who argued that the valence band in an energy from E_f to 1 eV below it is dominated by the electronic structure of the CoO₂ layer, with very little, if any, contribution from the RS subsystem. Our results presented so far are not in good agreement with this experimental observation, either, as we find that both subsystems contribute to the DOS at E_f . In fact, as shown in Fig. 4 and comparisons of Fig. 5 and 6, we observe that there is significantly more contribution to the DOS at E_f from the RS subsystem.

2. DOS Analysis within DFT+U

In searching for a possible explanation for this discrepancy, we considered the effect of electron correlations by including the on-site Coulomb interactions in the DFT+U formalism for the Co 3*d* orbitals. While we used a range of U values from 3 to 7 eV and also performed first principles computations of U using a linear response approach for Co atoms in both subsystems, in what follows we will present our results for $U = 5$ eV which is a reasonable value based on previous DFT studies on similar systems.^{44,45}

Figure 7 shows the total DOS for both spin channels computed for the 5/3 approximant with $U = 5$ eV. In contrast to the behavior displayed in Fig. 3 for $U = 0$, E_f now falls in a gap in the spin-down channel. CCO is still predicted to be a metal, since there is a small, but finite, DOS at E_f in the spin-up channel. As shown Fig. 8 which displays the Co 3*d* contributions from the two subsystems, the metallicity of CCO is now almost entirely due to the CoO₂ subsystem with a negligible contribution from the RS subsystem in the spin-up channel. Compared to behavior observed in Fig. 4, the inclusion of the Hubbard U , therefore, results in a significant change in the contributions from the RS subsystem to the DOS around E_f , while there is hardly any change in the contributions from the CoO₂ subsystem. Angular momentum resolved projections into various 3*d* orbitals belonging to the CoO₂ and RS subsystems (Fig. 9 and 10, respectively) also verify this; the only significant change for the CoO₂ subsystem is that the unoccupied e_g bands now lie ~ 2.3 eV above E_f (Fig. 9). For the RS subsystem, on the other hand, the e_g bands no longer contribute to the DOS at E_f , as they do for the $U = 0$ case. In addition, the only fully occupied m -resolved band in the spin-down channel is $d_{xy,\downarrow}$, and all the other previously ($U = 0$) partially occupied orbitals are now unoccupied (Fig. 10). These results show that inclusion of electron correlations beyond the mean-field description of DFT with a Hubbard U leads to agreement with experimental observations about the nature of states near E_f .^{14,19}

As is well-known, the energy correction introduced by the Hubbard U in the DFT+U method penalizes partial occupation of the localized orbitals, hence, favoring either fully occupied or empty orbitals. In the CoO₂ subsystem, since most of the states are already almost fully occupied (t_{2g}) or empty (e_g), the introduction of the Hubbard term leaves the nature of the states near E_f practically unchanged with the exception of increasing the band gap by ~ 1 eV. In the case of the RS subsystem on the other hand, several partially occupied states near E_f are split when the Hubbard U is introduced, placing E_f in a gap of Co 3*d* states. It is important to note that this does not mean that the electron correlations are less important in the CoO₂ subsystem. Our first principles computations for the magnitude of U using a linear response theory yield values of 5.4 and 8.1 eV for Co in the RS and CoO₂ sublattices, respectively. However, even such a large U value for the CoO₂ subsystem does not result in a significant change in the behavior of states near E_f , the only change being a slightly larger crystal field splitting between the t_{2g} and e_g states. What controls the position of E_f when U is introduced, is the energy gain due to the redistribution of the Co 3*d* bands from the RS subsystem to energies fully above and below E_f .

3. Evolution with respect to Approximant Size

Figures 11 and 12 show how the d projected PDOS around Co atoms in the CoO₂ and RS subsystems, respectively, evolve as a function of the approximant size. The results displayed are for $U = 5$ eV; the general trends as a function of approximant size do not change appreciably for other values of U including $U = 0$. As seen in Fig. 11, in the spin-

down channel E_f falls in a gap of PDOS projected into the d orbitals of the Co atoms in the CoO_2 subsystem (13/8 approximant is an exception to this, see below), while in the spin-up channel Co $3d$ states contribute significantly to the DOS at E_f giving rise to the metallic behavior. For projections into Co atoms in the RS subsystem (Fig. 12), again E_f lies in a gap of d states in the spin-down channel. In the spin-up channel, on the other hand, the PDOS at E_f remains quite small compared to the contribution from the CoO_2 subsystem, but is not zero. The smallest (almost zero) value of PDOS at E_f is obtained for the 5/3 approximant. For other approximants, the contribution increases in a non-monotonic fashion.

We have examined the reason behind the slight variations in the contributions to the DOS around E_f , in particular, from the RS subsystem, and find the answer in the details of the arrangements of the $(\text{Ca}_2\text{CoO}_3)$ RS structure into particular n -unit clusters, as discussed at the end of the last section. As might be inferred from the middle panel of the spin-up channel PDOS displayed in Fig. 10, the relevant orbital that gives rise to small contributions to DOS from the RS subsystem around E_f is $d_{3z^2-r^2}$. For the 5/3 approximation with an almost vanishing contribution to the DOS at E_f from the RS subsystem, there are two identical $(\text{Ca}_2\text{CoO}_3)_3$ clusters stacked along the b direction. Within each $(\text{Ca}_2\text{CoO}_3)_3$ cluster, two of the three Co atoms are symmetry-equivalent resulting in 2 distinct Co atoms. Of these two Co atoms, the Co-O interatomic distances for the rather distorted CoO_6 octahedra are such that when electron correlations are taken into account with a Hubbard U , for one of them the $d_{3z^2-r^2, \uparrow}$ orbital is fully occupied, while for the other, it is fully unoccupied and gives rise to the sharp peak observed ~ 1 eV above E_f . The formation of such fully occupied or unoccupied $e_{g, \uparrow}$ orbitals results in practically no contribution to the PDOS from the RS subsystem. However, any time the RS subsystem contains other types of clusters (such as the 1-, 2-, and 4-unit clusters) found in all other approximants, we observe that the Co atoms from such units contribute slightly to the DOS at E_f , as they are no longer able to accommodate the necessary number of electrons fully below E_f by neatly pairing up with other Co atoms in the relevant cluster, as they can do with a $(\text{Ca}_2\text{CoO}_3)_3$ cluster. Hence, we find that the (small) contributions to the DOS at E_f from the RS subsystem are correlated with the presence of 1-, 2-, and 4-unit clusters in them. The 13/8 approximant which contains the largest number of such clusters within one unit cell has, accordingly, a relatively large number of RS-derived e_g -like states in the vicinity of E_f . This analysis, along with the interpretations from the photoemission¹⁴ and transport¹⁹ experiments suggests that increasing the unit cell size along the incommensurate direction by going to larger and larger approximants may not necessarily lead to better models for CCO, and the “magic” 5/3 approximant does a good job for modeling the electronic properties of CCO, when correlations are taken into account.

C. Magnetic Properties

As mentioned earlier, our calculations were performed starting from a ferromagnetic initial configuration for all Co atoms in the structure. Since it is very common for these types of spin-polarized calculations to get trapped in local minima, especially when carried out within the DFT+U framework, we tested different initial magnetizations of 1.0, 1.3, 1.5, and $2 \mu_B$, in order to check the convergence to the correct ground state. Table V shows the final magnetic moments averaged over Co atoms in the RS and CoO_2 subsystems, in addition to the total magnetization per Co atom (M_{ave}) computed with different exchange-correlation functionals, $U = 0$ and 5 eV, for all rational approximants considered. The magnetization primarily arises from Co atoms in the RS subsystem; the average magnetic moment in the CoO_2 subsystem is at least one order of magnitude smaller than that in the RS subsystem. The value of M_{ave} increases when the calculations are performed within the DFT+U framework compared to the corresponding regular DFT calculation. Furthermore, M_{ave} computed with PBE is always larger than that computed with the LDA exchange-correlation functional for both $U = 0$ and 5 eV, however, the difference between PBE+U and LDA+U values for M_{ave} is considerably less compared to that between the PBE and LDA values. This is the same observation we reported earlier for the structural parameters, in particular, for the predicted fractional coordinates. If we consider the trends as a function of the approximant size, we observe that the convergence is fairly fast, *e.g.* at the LDA level, the M_{ave} values for the 3/2, 5/3, 8/5, and 13/8 rational approximants are 0.78, 0.88, 0.89, and $0.87 \mu_B$, respectively. The computed M_{ave} that seems to have converged to a value near $0.88 \mu_B$ is underestimated compared to the experimentally measured value near $1.3 \mu_B$ for temperatures of less than 400 K.¹⁰ Within LDA+U, on the other hand, the computed M_{ave} (for $U = 5$ eV) are 1.34, 1.19, 1.24, and $1.29 \mu_B$, respectively, converging to a value near $1.3 \mu_B$, in excellent agreement with the experimentally reported value. These results show that the inclusion of electron correlations within DFT+U improves the agreement with experiment regarding not only the contribution of the two subsystems to the DOS near E_f but also the computed magnetic moments as well.

D. Seebeck Coefficient of CCO

The results from the DOS analysis presented above can be used to obtain an estimate for the Seebeck coefficient (thermopower) S of CCO within the framework of Heikes formula:⁴⁸

$$S = -\frac{k_B}{e} \ln \left(\frac{g_3}{g_4} \frac{x}{1-x} \right), \quad (1)$$

where x is the concentration of Co^{4+} ions, and g_3 and g_4 the degeneracies (including both spin and orbital degrees of freedom) for the Co^{3+} and Co^{4+} , respectively. Based on our results for the 5/3 approximant with $U = 5$ eV, we assume that S is determined solely by the contribution from the CoO_2 subsystem. As inferred from Fig. 9, the Co atoms in the CoO_2 subsystem are in a low-spin (LS) configuration, and in a mixed-valence state of Co^{3+} ($t_{2g,\uparrow}^3 e_{g,\uparrow}^0$) and Co^{4+} ($t_{2g,\uparrow}^2 e_{g,\uparrow}^0$). We determine the concentration x from ratio of unoccupied $t_{2g,\uparrow}$ PDOS to the whole area under the $t_{2g,\uparrow}$ PDOS curve from ~ -1.5 eV to ~ 0.2 eV, averaging over the three orbitals. We find a value near 0.3. Setting the degeneracies for the LS configurations of Co^{3+} and Co^{4+} as $g_3 = 1$ and $g_4 = 6$, we thus arrive at a value for $S \sim 227 \mu\text{VK}^{-1}$.

Our computed value for S is significantly larger than the value of $41 \mu\text{VK}^{-1}$ obtained by Asahi *et al.*³⁵ in their analysis of CCO using the 3/2 approximant. The reason for the large discrepancy can readily be attributed to the differences in the electronic structures of CCO as obtained in the respective first principles studies. In particular, Asahi *et al.* assume no contribution to the Seebeck coefficient from the CoO_2 subsystem, as E_f falls in crystal-field gap of Co d states in the CoO_2 subsystem, and the contribution from the RS subsystem is computed using x , g_3 , and g_4 as inferred from their ($U = 0$) calculation. As mentioned before, these findings of Asahi *et al.* are not in agreement with results from the photoemission experiments of Takeuchi *et al.* This observation led us to consider electron correlations within a DFT+ U framework that indeed led to the finding of a vanishing DOS at E_f from the RS subsystem. Even with this improvement, the agreement of our computed value for $S \sim 227 \mu\text{VK}^{-1}$ with the experimental values near $135 \mu\text{VK}^{-1}$ (Refs. 10, 15, and 26) is only somewhat fair. However, one should take into account the fact that S has a rather sensitive dependence on x . For example, a value of $x = 0.56$ would result in perfect agreement with experiment. The concentration of Co^{4+} ions was indeed inferred to be $x \sim 0.5$ in recent electron energy-loss spectroscopy studies of Yang *et al.*,²¹ who reported an average Co valence of 3.5 in the CoO_2 subsystem. One should also keep in mind that the computations are based on the pristine 5/3 approximant model of CCO, and defects and unintentional doping in real materials could change the measured Seebeck coefficient significantly. Finally, we note that our value of $x \sim 0.3$, while not leading to very good agreement with experiment for the values of S as described above, is rather consistent with the amount of doping (interpreted as Co^{4+} content) obtained from transport measurements of Limelette *et al.*¹⁶ and Eng *et al.*¹⁹ who find values near 0.32 and 0.36, respectively. In future studies, it would be instructive to use the computed band structure directly within Boltzmann transport formalism⁵¹ in order to obtain an independent estimate of the Seebeck coefficient.

IV. SUMMARY

We have reported results on and analyses of first principles calculations, performed within the framework of standard DFT and DFT+ U , for misfit-layered CCO modeled by rational approximants with systematically increasing unit cell sizes. The structural parameters computed within DFT and DFT+ U are found to be in reasonably good agreement with experimental values and previous computations. The standard DFT calculations predict a large contribution to the DOS at E_f from the RS subsystem, in disagreement with results from photoemission experiments. When electron correlations are taken into account within a DFT+ U formalism, d states derived from Co atoms in the RS subsystem are observed to have very little, if any, contribution to DOS at E_f , and the states that give rise to the metallic conductivity of CCO are essentially all derived from Co atoms in the hexagonal CoO_2 subsystem, in agreement with results from photoemission data. It is interesting to note that even though our first principles linear response calculations for the Hubbard U indicate a value for Co atoms belonging to the CoO_2 subsystem (8.1 eV) that is significantly larger than that for Co atoms in the RS subsystem (5.4 eV), the introduction of U does not result in a significant change in the nature of states derived from the Co atoms in the CoO_2 subsystem, since the relevant t_{2g} states associated with the CoO_2 subsystem are nearly fully occupied and the e_g states fully unoccupied. The impact of U on the RS subsystem, on the other hand, is significant as it opens up a gap in the partial DOS at E_f . Our results, therefore, strongly suggest that the necessary ingredient for obtaining agreement with photoemission experiments is to take the correlations into account in the RS subsystem. The size of the rational approximant as a structural model for the incommensurate CCO plays a minor role in this regard. In particular, even a relatively small 5/3 approximant does a good job in modeling the essential electronic properties of CCO. We have presented results

that associate the opening of the gap in the PDOS of Co atoms belonging to the RS subsystem with the formation of particular structural features in the form of $(\text{Ca}_2\text{CoO}_3)_n$ clusters that extend along the incommensurate b -direction. We have also shown that another significant effect of U is to bring the computed magnetic moments per Co atom in nearly perfect agreement with experimental values and to minimize the differences between the predictions of LDA+U and PBE+U. Based on our DOS analysis, we find the Co atoms that contribute to the metallic conductivity in CCO (i.e. those in the CoO_2 subsystem) to be in a mixture of Co^{3+} and Co^{4+} low-spin configurations, with a predicted concentration near 30% for Co^{4+} ions. While this value is in very good agreement with results from transport measurements, the predicted Seebeck coefficient S using this concentration of Co^{4+} ions and Heikes formula has only a fair agreement with experimentally measured values for S . We expect that further refinements of the structural models for CCO, more sophisticated approaches for treating electron correlations, and incorporating energetically favorable point and extended defects in modeling studies will likely lead to the successful resolution of the slight discrepancies remaining between experiment and theory for this technologically and scientifically important oxide thermoelectric material.

ACKNOWLEDGMENTS

We acknowledge support for this work by the National Science Foundation under Grant No. DMR-0846746 (R.F.K) and partial support by the Department of Energy under Grant No. DE-FG02-09ER16072 (A.R.). P.Z. acknowledges support from the U.S. Department of Energy BES-Materials Sciences under Contract DE-AC0206CH11357. S.Ö acknowledges support by the National Science Foundation under the Independent Research/Development program while working at the Foundation. This research used resources of NERSC, which is supported by the Office of Science of the U.S. Department of Energy.

-
- ¹ A. Ohtomo, D. A. Muller, J. L. Grazul, and H. Y. Hwang, *Nature* **419**, 378 (2002).
 - ² S. Okamoto and A. J. Millis, *Nature* **428**, 630 (2004).
 - ³ I. Terasaki, Y. Sasago, and K. Uchinokura, *Phys. Rev. B* **56**, 12685 (1997).
 - ⁴ L. Seguin, G. Amatucci, M. Anne, Y. Chabre, P. Strobel, J. M. Tarascon, G. Vaughan, *J. Power Sources* **81-82**, 604 (1999).
 - ⁵ R. Funahashi and Ichiro Marsubara, *Appl. Phys. Lett.* **79**, 362 (2001).
 - ⁶ I. Matsubara, R. Funahashi, M. Shikano, K. Sasaki, H. Enomoto, *Appl. Phys. Lett.* **80**, 4729 (2002).
 - ⁷ Y. Wang, N. S. Rogado, R. J. Cava, and N. P. Ong, *Nature* **423**, 428 (2003).
 - ⁸ J. Androulakis, P. Migiakis, and J. Giapintzakis, *Appl. Phys. Lett.* **84**, 1099 (2004).
 - ⁹ M. Shizuya, M. Isobe, Y. Baba, T. Nagai, M. Osada, K. Kosuda, S. Takenouchi, Y. Matsui, E. Takayama-Muromachi, *J. Sol. Stat. Chem.* **180**, 249 (2007).
 - ¹⁰ A. C. Masset, C. Michel, A. Maignan, M. Hervieu, O. Toulemonde, F. Studer, B. Raveau, and J. Hejtmanek, *Phys. Rev. B* **62**, 166 (2000).
 - ¹¹ Y. Miyazaki, M. Onoda, T. Oku, M. Kikuchi, Y. Isui, Y. Ono, Y. Morii, and T. Kajitani, *J. Phys. Soc. Jpn.* **71**, 491 (2002).
 - ¹² J. Sugiyama, J. H. Brewer, E. J. Ansaldo, H. Itahara, K. Dohmae, Y. Seno, C. Xia, and T. Tani, *Phys. Rev. B* **68**, 134423 (2003).
 - ¹³ W. Seo, S. Lee, Y. Lee, M. Lee, Y. Masuda and K. Koumoto, *J. Elect. Micr.* **53**, 397 (2004).
 - ¹⁴ T. Takeuchi, T. Kondo, T. Takami, H. Takahashi, H. Ikuta, U. Mizutani, K. Soda, R. Funahashi, M. Shikano, M. Mikami, S. Tsuda, T. Yokoya, S. Shin, T. Muro, *Phys. Rev. B* **69**, 125410 (2004).
 - ¹⁵ Y. F. Hu, W. D. Si, E. Sutter, and Q. Li, *Appl. Phys. Lett.* **83**, 082103 (2005).
 - ¹⁶ P. Limelette, V. Hardy, P. Auban-Senzier, D. Jérôme, D. Flahaut, S. Hébert, R. Frésard, Ch. Simon, J. Noudem, and A. Maignan, *Phys. Rev. B* **71**, 233108 (2005).
 - ¹⁷ S. Bhattacharya, D. K. Aswal, A. Singh, C. Thinaharan, N. Kulkarni, S. K. Gupta, J. V. Yakhmi, *J. Crys. Growth* **277**, 246 (2005).
 - ¹⁸ T. Burnus, Z. Hu, M. W. Haverkort, J. C. Cezar, D. Flahaut, V. Hardy, A. Maignan, N. B. Brookes, A. Tanaka, H. H. Hsieh, H. -J. Lin, C. T. Chen, and L. H. Tjeng, *Phys. Rev. B* **74**, 245111 (2006).
 - ¹⁹ H. W. Eng, P. Limelette, W. Prellier, Ch. Simon, and R. Frésard, *Phys. Rev. B* **73**, 033403 (2006).
 - ²⁰ M. S. Dresselhaus, G. Chen, M. Y. Tang, R. Yang, H. Lee, D. Wang, Z. Ren, J.-P. Fleurial, and P. Gogna, *Adv. Mater.* **19**, 1043 (2007).
 - ²¹ G. Yang, R. F. Klie, Q. Ramasse, *Phys. Rev. B* **78**, 153109 (2008).
 - ²² H. Muguerra, D. Grebille, and F. Bourée, *Acta Crys.* **B64**, 144 (2008).
 - ²³ Y. Wakisaka, S. Hirata, T. Mizokawa, Y. Suzuki, Y. Miyazaki, and T. Kajitani, *Phys. Rev. B* **78**, 235107 (2008).
 - ²⁴ T. A. Tyson, Z. Chen, Q. Jie, Q. Li, and J. J. Tu, *Phys. Rev. B* **79**, 024109 (2009).
 - ²⁵ T. Sun, J. Ma, Q. Y. Yan, Y. Z. Huang, J. L. Wang, H. H. Hng, *J. Crys. Growth* **311**, 4123 (2009).
 - ²⁶ Q. Qiao, A. Güleş, T. Paulauskas, S. Kolesnik, B. Dabrowski, M. Özdemir, C. Boyraz, D. Mazumdar, A. Gupta, and R. F. Klie, *J. Phys. Condens. Matter* **23**, 305005 (2011).
 - ²⁷ I. Matsubara, R. Funahashi, M. Shikano, K. Sasaki, and H. Enomoto, *Appl. Phys. Lett.* **80**, 4729 (2002).
 - ²⁸ G. Xu, R. Funahashi, M. Shikano, I. Matsubara, and Y. Zhou, *Appl. Phys. Lett.* **80**, 3760 (2002).
 - ²⁹ D. Wang, L. Chen, Q. Yao, J. Li, *Solid State Comm.* **129**, 615 (2004).
 - ³⁰ H. Q. Liu, X. B. Zhao, T. J. Zhu, Y. Song, F. P. Wang, *Curr. Appl. Phys.* **9**, 409 (2009).
 - ³¹ L. Xu, F. Li, Y. Wang, *J. Alloys Compd.* **501**, 115 (2010).
 - ³² G. D. Tang, Z. H. Wang, X. N. Xu, L. Qiu, L. Xing, Y. W. Du, *J. Mater. Sci.* **45**, 3969 (2010).
 - ³³ G. D. Tang, X. N. Xu, C. P. Tang, Z. H. Wang, Y. He, L. Qiu, L. Y. Lv, L. Xing and Y. W. Du, *Europhys. Lett.* **91**, 17002 (2010).
 - ³⁴ T. Sun, H. H. Hng, Q. Y. Yan, and J. Ma, *J. Appl. Phys.* **108**, 083709 (2010).
 - ³⁵ R. Asahi, J. Sugiyama, and T. Tani, *Phys. Rev. B* **66**, 155103 (2002).
 - ³⁶ G. D. Tang, H. H. Guo, T. Yang, D. W. Zhang, X. N. Xu, L. Y. Wang, Z. H. Wang, H. H. Wen, Z. D. Zhang, and Y. W. Du, *Appl. Phys. Lett.* **98**, 202109 (2011).
 - ³⁷ D. P. DiVincenzo and P. J. Steinhardt, *Quasicrystals: The State of the Art* (World Scientific, Singapore, 1991).
 - ³⁸ V. I. Anisimov, J. Zaanen, and O. K. Andersen, *Phys. Rev. B* **44**, 943 (1991).
 - ³⁹ V. I. Anisimov, I. V. Solov'ev, M. A. Korotin, M. T. Czyzyk, and G. A. Sawatzky, *Phys. Rev. B* **48**, 16929 (1993).
 - ⁴⁰ G. Kresse and J. Hafner, *Phys. Rev. B* **47**, 558 (1993); P. E. Blöchl, *ibid.* **50**, 17953 (1994).
 - ⁴¹ D. M. Ceperley and B. J. Alder, *Phys. Rev. Lett.* **45**, 566 (1980).
 - ⁴² J. P. Perdew, K. Burke, and M. Ernzerhof, *Phys. Rev. Lett.* **77**, 3865 (1996).
 - ⁴³ S. L. Dudarev, G. A. Botton, S. Y. Savrasov, C. J. Humphreys and A. P. Sutton, *Phys. Rev. B* **57**, 1505 (1998).
 - ⁴⁴ D. J. Singh, *Phys. Rev. B* **61**, 13397 (2000).
 - ⁴⁵ P. Zhang, W. Luo, V. H. Crespi, M. L. Cohen, and S. G. Louie, *Phys. Rev. B* **70**, 085108 (2004).
 - ⁴⁶ M. Cococcioni and S. de Gironcoli, *Phys. Rev. B* **71**, 035105 (2005).
 - ⁴⁷ P. Gianozzi *et al.*, *J. Phys.: Condens. Matter* **21**, 395502 (2009).
 - ⁴⁸ W. Koshibae, K. Tsutsui, and S. Maekawa, *Phys. Rev. B* **62**, 6869 (2000).
 - ⁴⁹ A. Maignan, S. Hébert, D. Pelloquin, C. Michel and J. Hejtmanek, *J. Appl. Phys.* **92**, 1964 (2002).

- ⁵⁰ Y. Zhou, I. Matsubara, S. Horii, T. Takeuchi, R. Funahashi, M. Shikano, J. Shimoyama, K. Kishio, W. Shin, N. Izu, and N. Murayama, *J. Appl. Phys.* **93**, 2653 (2003).
- ⁵¹ G. K. H. Madsen and D. J. Singh, *Comp. Phys. Comm.* **175**, 67 (2006).

TABLE I. Experimental and computed (within DFT) lattice parameters for all the rational approximants. The lengths of the lattice parameters are given in Å.

Approximant	a	b_{RS}	b_{CoO_2}	c	β
3/2 (LDA)	4.73	4.29	2.86	10.52	98.13°
3/2 (PBE)	4.89	4.39	2.92	10.92	98.14°
5/3 (LDA)	4.75	4.57	2.74	10.50	98.31°
8/5 (LDA)	4.76	4.47	2.79	10.50	98.25°
13/8 (LDA)	4.76	4.50	2.77	10.48	98.28°
Experimental	4.83	4.56	2.82	10.84	98.13°

TABLE II. Experimental and computed (within DFT) fractional coordinates for all the rational approximants. See Fig. 1 for the atom labels. Unless otherwise noted, all results are from computations performed within LDA.

Subsystem	Atom	Experimental		3/2		3/2 (PBE)		5/3		8/5		13/8	
		a	c	a	c	a	c	a	c	a	c	a	c
CoO ₂	Co	0.000	0.000	0.000	0.000	0.000	0.000	0.000	0.000	0.000	0.000	0.000	0.000
	O1	0.363	0.084	0.363	0.089	0.364	0.090	0.363	0.093	0.364	0.092	0.363	0.093
	O2	0.636	0.896	0.632	0.907	0.636	0.910	0.637	0.907	0.636	0.908	0.637	0.907
RS	Ca1	0.182	0.281	0.174	0.272	0.179	0.276	0.173	0.278	0.177	0.276	0.176	0.277
	Ca2	0.312	0.727	0.313	0.724	0.317	0.724	0.314	0.722	0.317	0.724	0.316	0.723
	Co	0.702	0.505	0.794	0.498	0.799	0.500	0.799	0.500	0.799	0.500	0.800	0.500
	O1	0.718	0.338	0.689	0.329	0.691	0.333	0.691	0.333	0.694	0.333	0.693	0.333
	O2	0.183	0.497	0.188	0.498	0.203	0.500	0.182	0.500	0.180	0.500	0.179	0.500
	O3	0.837	0.677	0.795	0.666	0.799	0.667	0.799	0.667	0.801	0.667	0.800	0.667

TABLE III. Experimental and computed (within DFT+U) lattice parameters for all the rational approximants using $U = 5$ eV. The lengths of the lattice parameters are given in Å.

Approximant	a	b_{RS}	b_{CoO_2}	c	β
3/2 (LDA+U)	4.75	4.24	2.83	10.65	98.20°
3/2 (PBE+U)	4.81	4.34	2.89	10.86	98.11°
5/3 (LDA+U)	4.75	4.58	2.75	10.54	98.34°
8/5 (LDA+U)	4.74	4.46	2.79	10.58	98.28°
13/8 (LDA+U)	4.76	4.50	2.77	10.58	98.28°
Experimental	4.83	4.56	2.82	10.84	98.13°

TABLE IV. Experimental and computed (within DFT+U) fractional coordinates for all the rational approximants using $U = 5$ eV. See Fig. 1 for the atom labels. Unless otherwise noted, all results are from computations performed within LDA+U.

Subsystem	Atom	Experimental		3/2		3/2 (PBE+U)		5/3		8/5		13/8	
		a	c	a	c	a	c	a	c	a	c	a	c
CoO ₂	Co	0.000	0.000	0.000	0.000	0.000	0.000	0.000	0.000	0.000	0.000	0.000	0.000
	O1	0.363	0.084	0.365	0.093	0.366	0.093	0.364	0.095	0.365	0.094	0.364	0.094
	O2	0.636	0.896	0.635	0.907	0.634	0.907	0.636	0.906	0.635	0.906	0.636	0.906
RS	Ca1	0.182	0.281	0.175	0.268	0.178	0.274	0.174	0.275	0.178	0.273	0.176	0.273
	Ca2	0.312	0.727	0.318	0.732	0.317	0.724	0.316	0.725	0.320	0.727	0.319	0.727
	Co	0.702	0.505	0.797	0.500	0.794	0.500	0.794	0.500	0.799	0.500	0.795	0.500
	O1	0.718	0.338	0.688	0.335	0.687	0.333	0.687	0.335	0.691	0.334	0.691	0.336
	O2	0.183	0.497	0.212	0.500	0.211	0.500	0.206	0.500	0.208	0.500	0.207	0.500
	O3	0.837	0.677	0.793	0.665	0.793	0.667	0.795	0.665	0.798	0.666	0.797	0.665

TABLE V. Averaged magnetic moments (in μ_B) for Co atoms belonging to the RS and CoO₂ subsystems and averaged magnetic moment per cell per Co (M_{ave}) for the different approximants, performed within standard DFT and DFT+U, with LDA and PBE exchange-correlation functionals. The value of the Hubbard parameter is $U = 5$ eV.

Approximant	Ex-corr	RS	CoO ₂	M_{ave}
3/2	LDA	1.66	-0.11	0.78
	LDA+U	2.76	-0.03	1.34
3/2	PBE	2.26	0.18	1.26
	PBE+U	2.94	0.10	1.49
5/3	LDA	1.50	0.22	0.88
	LDA+U	2.75	-0.13	1.19
5/3	PBE	2.08	0.12	1.07
	PBE+U	2.86	-0.16	1.19
8/5	LDA	1.53	0.19	0.89
	LDA+U	2.77	-0.10	1.24
13/8	LDA	1.48	0.20	0.87
	LDA+U	2.71	0.00	1.29

FIG. 2. (Color online) The relaxed structures (with $U = 5$ eV) of all approximants along the a direction. Each structure shows one unit cell plus an extra CoO₂ layer along the c direction. The structural patterns, mentioned in the text, composed of n -unit $X \equiv \text{Ca}_2\text{CoO}_3$ clusters that occur along the b direction are clearly visible. Representatives for $n = 1, 2, 3$, and 4 are shown with dashed ellipses and denoted as X_n .

FIG. 3. (Color online) Total DOS (showing spin-up and spin-down channels) computed for the 5/3 rational approximant. The lower panel shows the details of the total DOS within ± 4 eV of the Fermi level, which is denoted by the (red) vertical dashed line.

FIG. 4. (Color Online) Partial DOS projected into d -orbitals of Co atoms in the CoO₂ (upper panels) and the RS (lower panels) subsystems in the spin-up (left) and spin-down (right) channels. The Fermi level is shown with the (red) vertical dashed lines.

FIG. 1. (Color online) The structure of the unrelaxed 5/3 rational approximant of CCO (one unit cell plus an extra CoO₂ layer) along the b (left) and a (right) directions. The large gray, medium-sized dark (red), and small white circles represent Ca, Co, and O atoms, respectively. The particular atoms in CoO₂ and RS subsystems with fractional coordinates given in Tables II and IV are labeled on the left. The periodicities b_{CoO_2} and b_{RS} of the CoO₂ and RS subsystems are shown on the right.

FIG. 5. (Color Online) Spin-up (left) and spin-down (right) partial DOS projected into m -resolved d -orbitals of Co atoms in the CoO₂ subsystem. The Fermi level is shown with the (red) vertical dashed lines.

FIG. 6. (Color Online) Spin-up (left) and spin-down (right) partial DOS projected into m -resolved d -orbitals of Co atoms in the RS subsystem. The Fermi level is shown with the (red) vertical dashed lines.

FIG. 7. (Color online) Total DOS (showing spin-up and spin-down channels) computed for the 5/3 rational approximant within LDA+U. The Fermi level is shown by the (red) vertical dashed line. The calculations are performed with $U = 5$ eV.

FIG. 8. (Color Online) Partial DOS, computed with LDA+U, projected into d -orbitals of Co atoms in the CoO₂ (upper panels) and the RS (lower panels) subsystems in the spin-up (left) and spin-down (right) channels. The Fermi level is shown with the (red) vertical dashed lines. The calculations are performed with $U = 5$ eV.

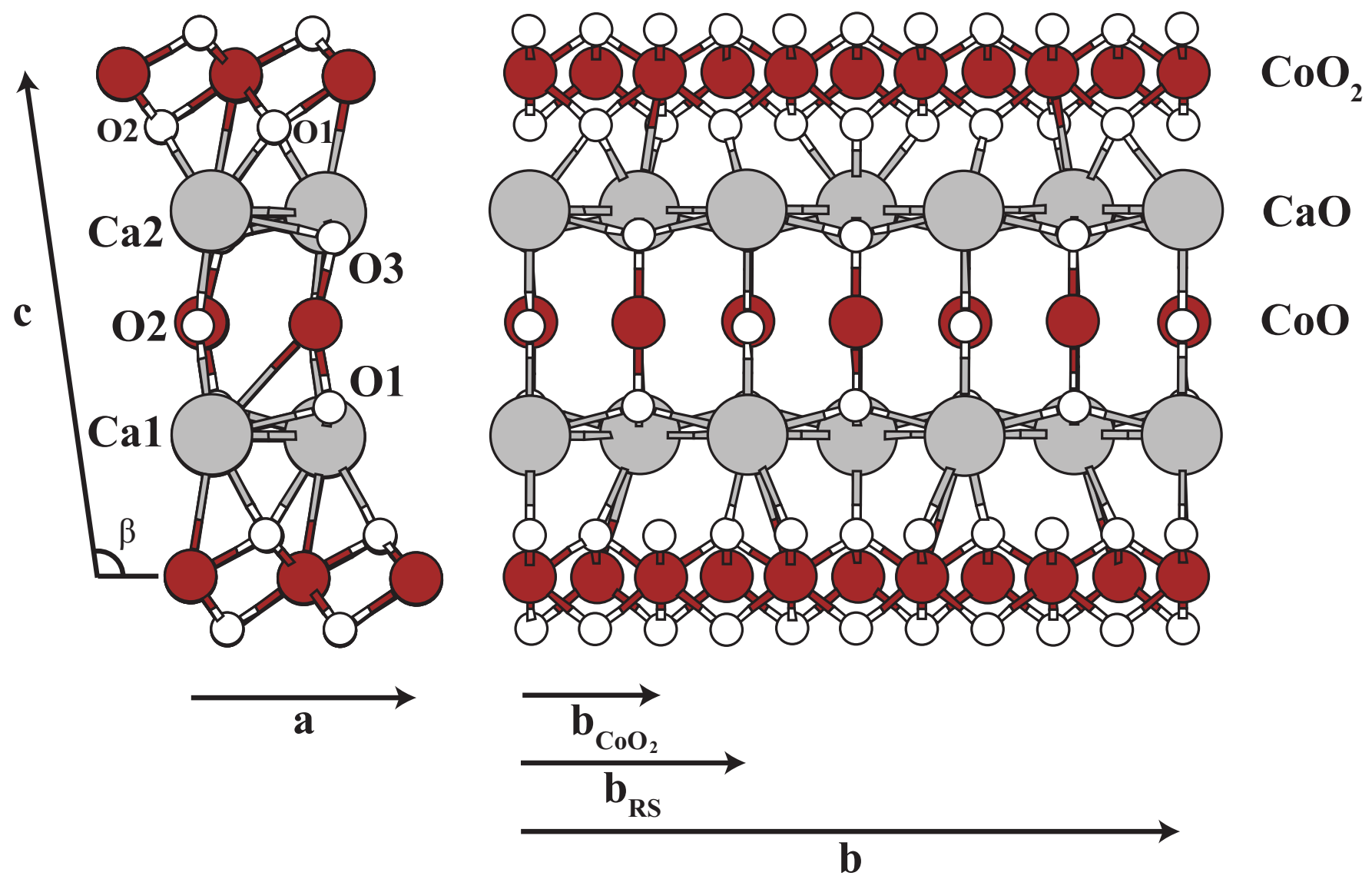
FIG. 9. (Color Online) Spin-up (left) and spin-down (right) partial DOS, computed within LDA+U, projected into m -resolved d -orbitals of Co atoms in the CoO₂ subsystem. The Fermi level is shown with the (red) vertical dashed lines. The calculations are performed with $U = 5$ eV.

FIG. 10. (Color Online) Spin-up (left) and spin-down (right) partial DOS, computed within LDA+U, projected into m -resolved d -orbitals of Co atoms in the RS subsystem. The Fermi level is shown with the (red) vertical dashed lines. The calculations are performed with $U = 5$ eV.

FIG. 11. (Color Online) Partial DOS, computed within LDA+U, projected into d -orbitals averaged over all Co atoms in the CoO₂ subsystem for the 3/2, 5/3, 8/5 and 13/8 rational approximants. The Fermi level is shown with the (red) vertical dashed lines. The calculations are performed with $U = 5$ eV.

FIG. 12. (Color Online) Partial DOS, computed within LDA+U, projected into d -orbitals averaged over all Co atoms in the RS subsystem for the 3/2, 5/3, 8/5 and 13/8 rational approximants. The Fermi level is shown with the (red) vertical dashed lines. The calculations are performed with $U = 5$ eV.

Figure 1 BN11985 26Mar2012



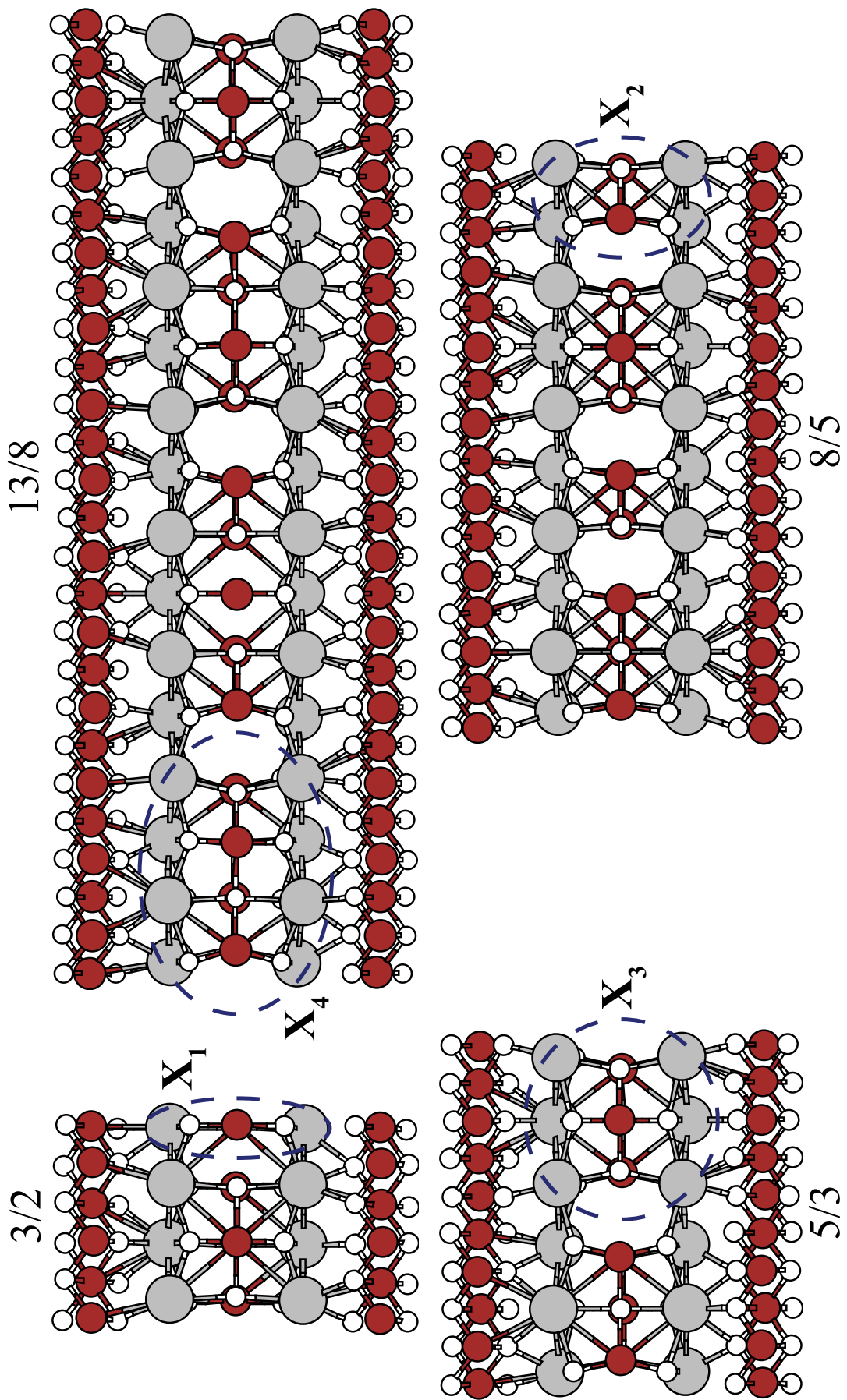


Figure 2 BN11985 26Mar2012

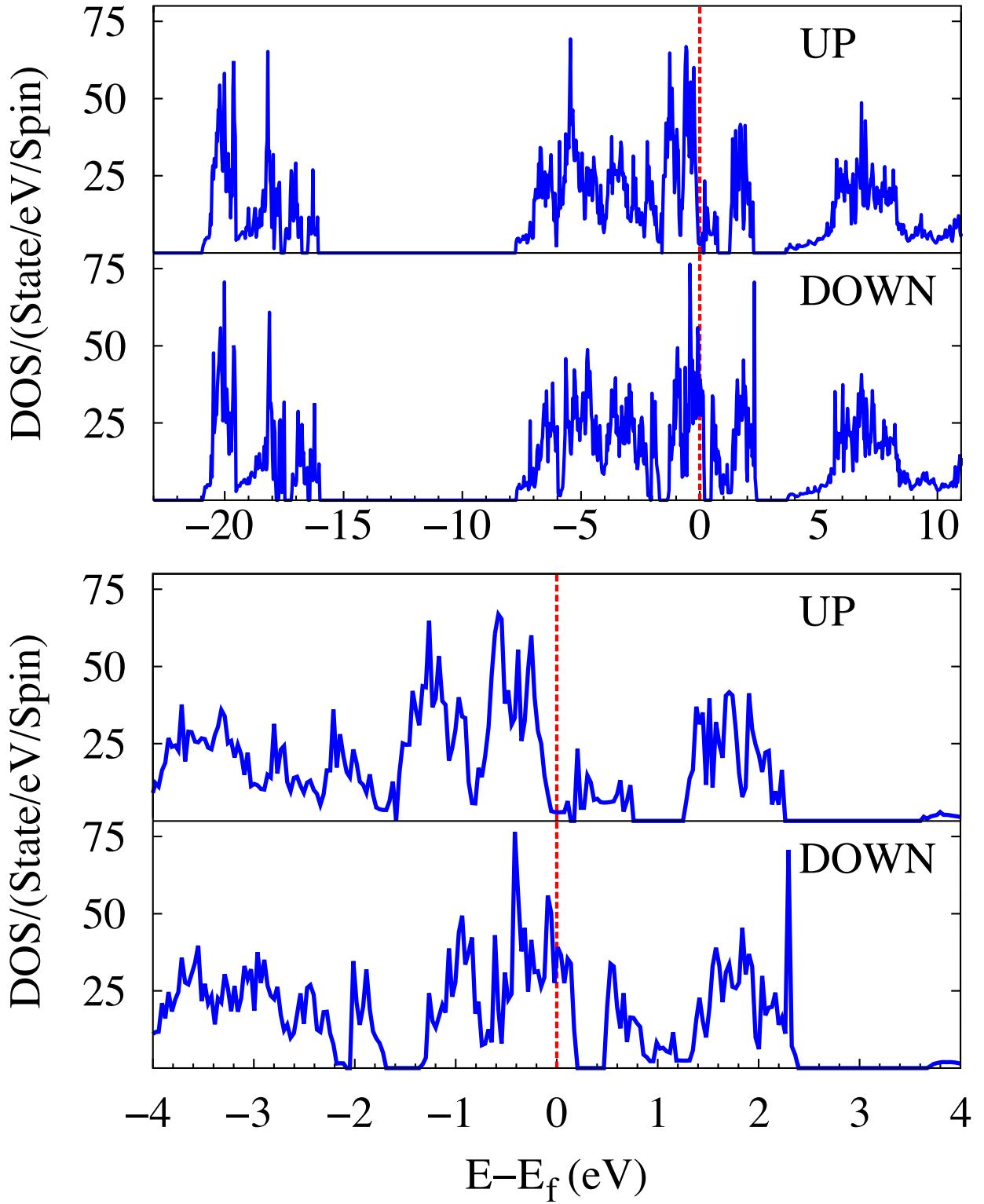


Figure 3

BN11985

26Mar2012

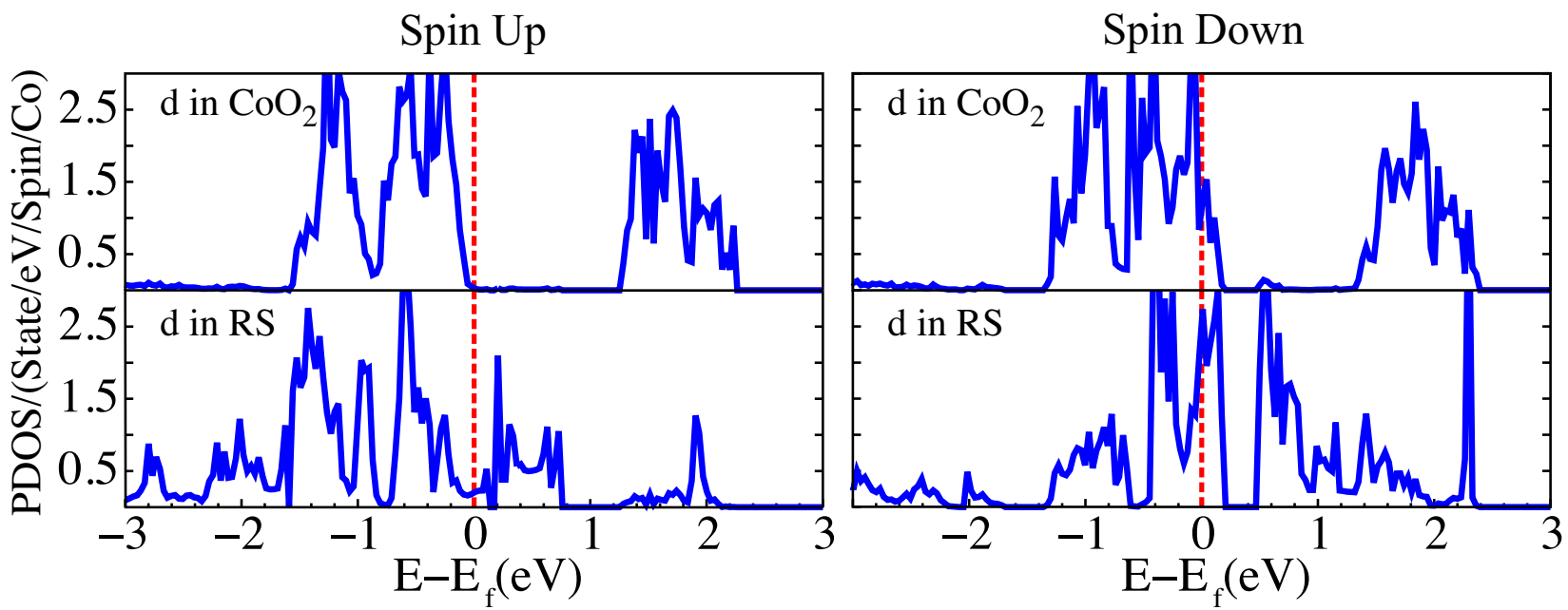


Figure 4

BN11985

26Mar2012

Figure 5 BN11985 26Mar2012

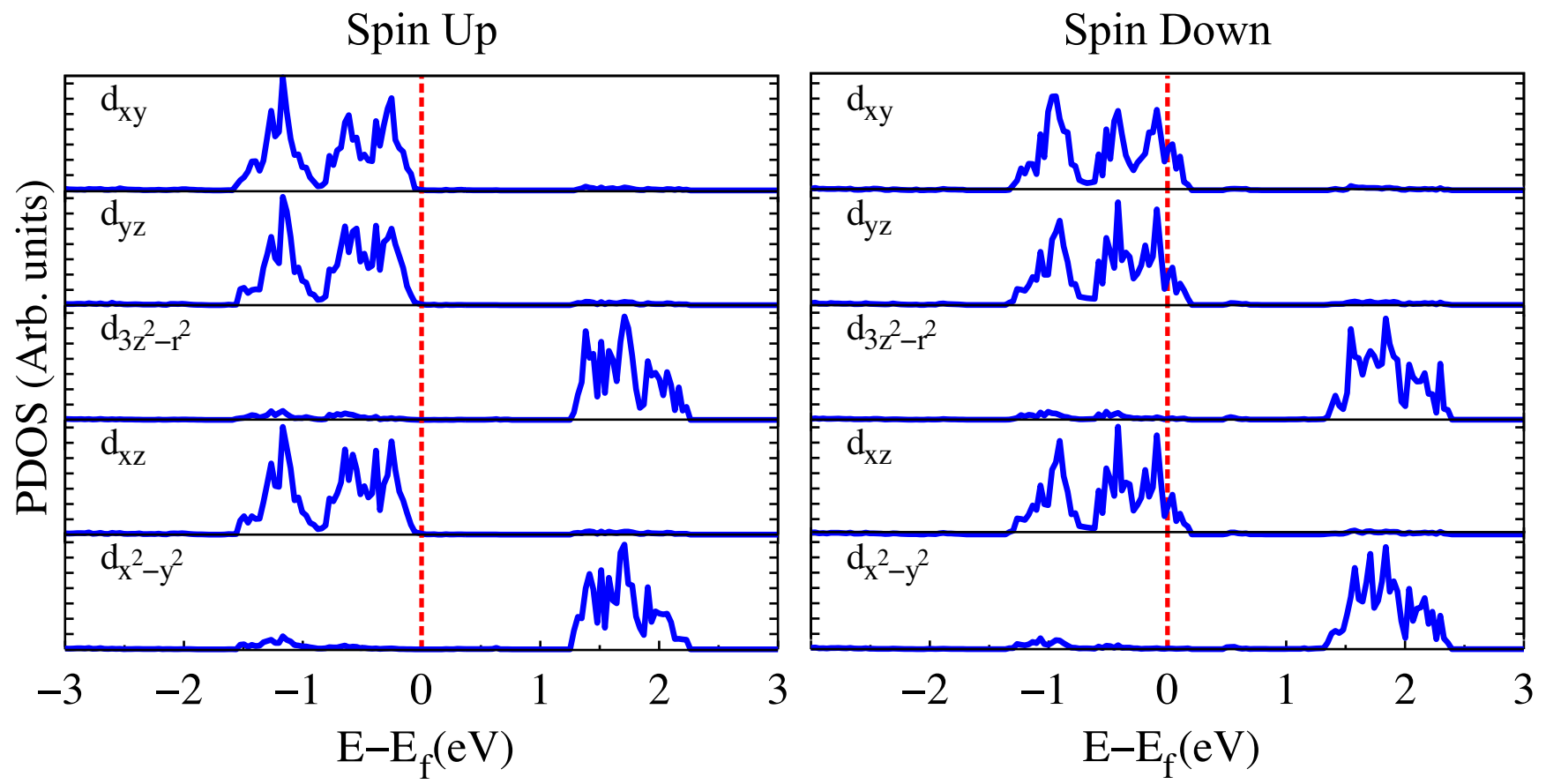


Figure 6 BN11985 26Mar2012

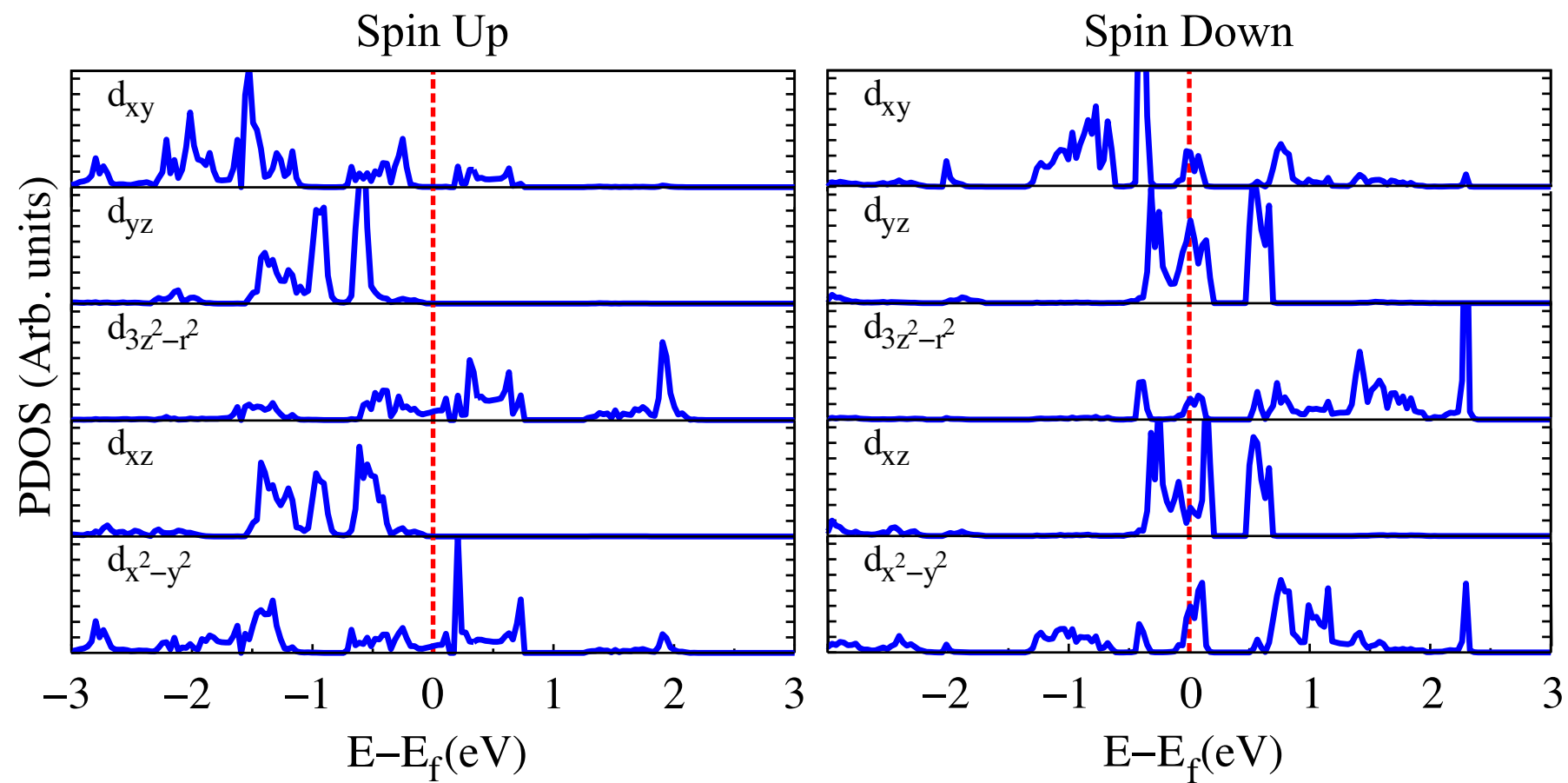


Figure 7 BN11985 26Mar2012

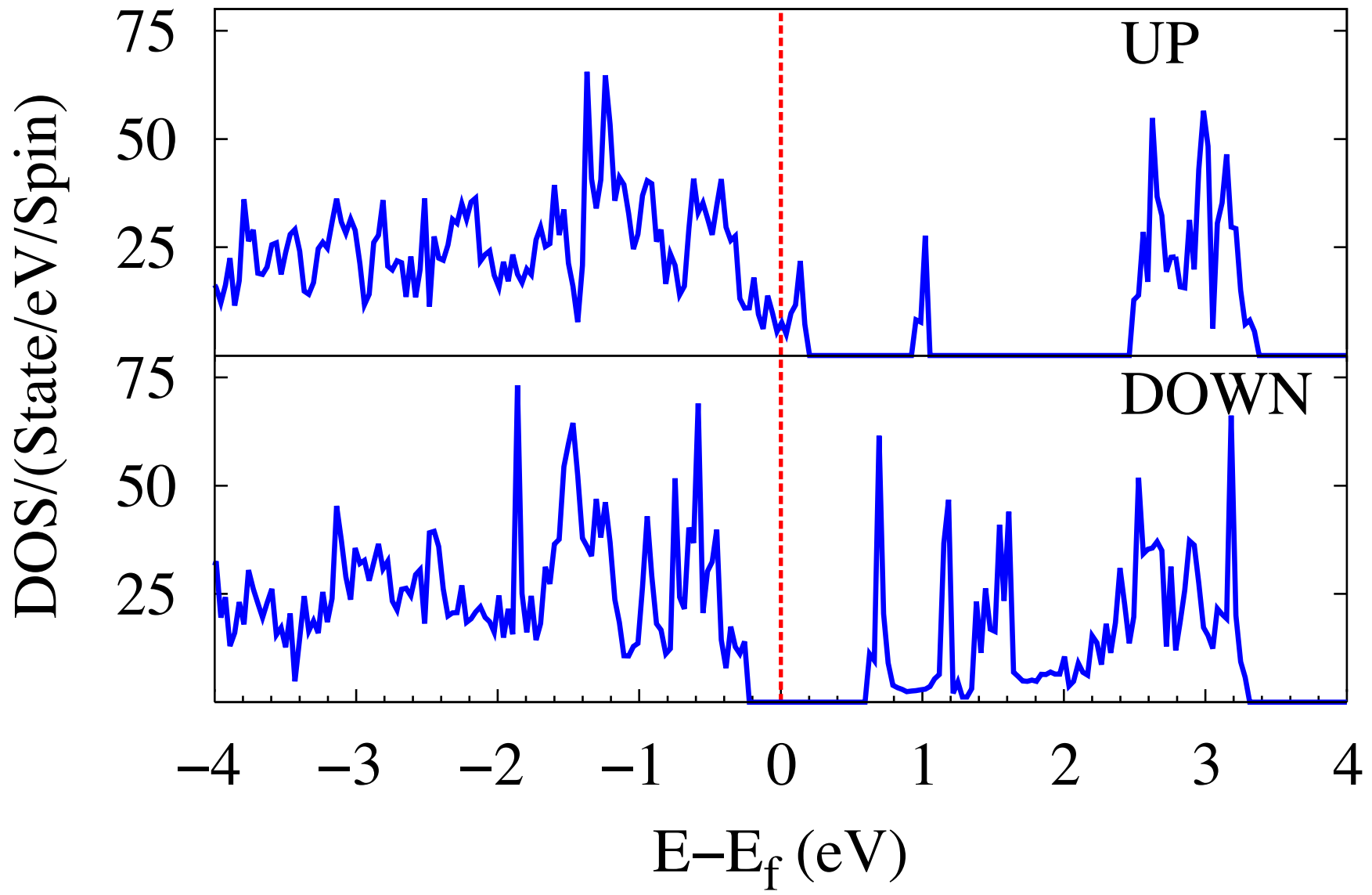


Figure 8 BN11985 26Mar2012

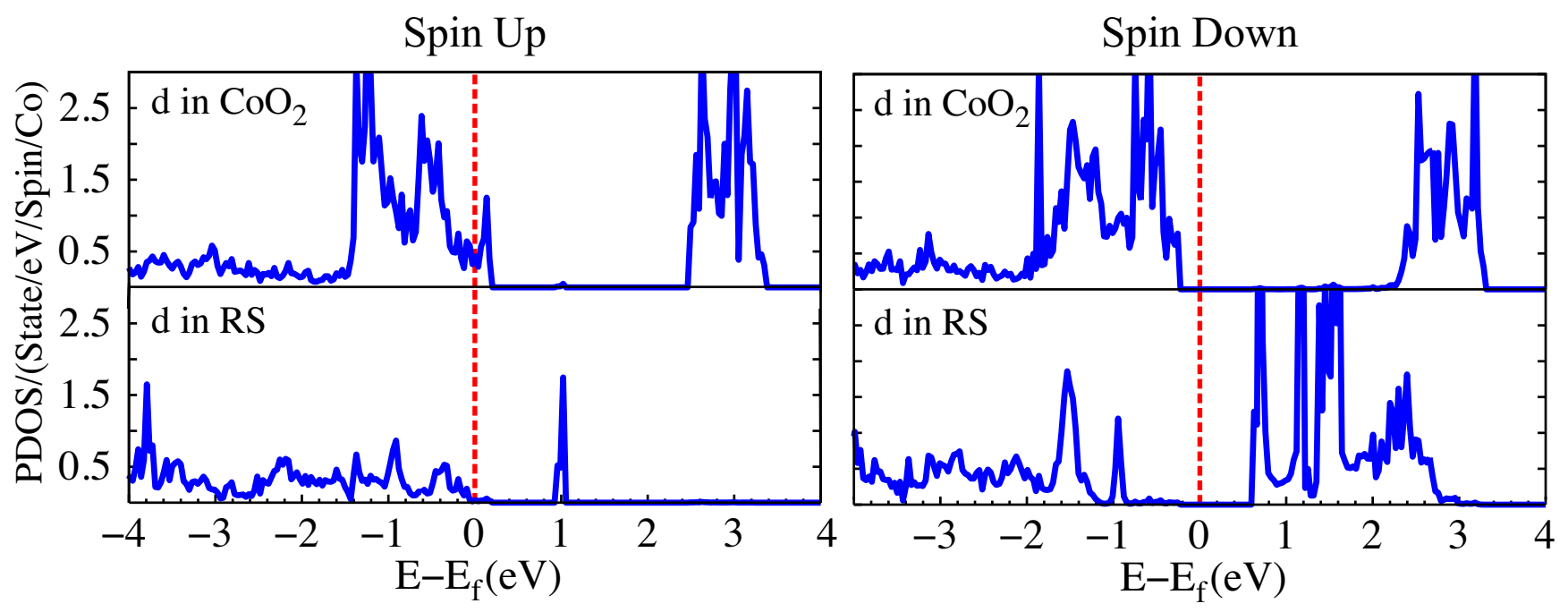


Figure 9 BN11985 26Mar2012

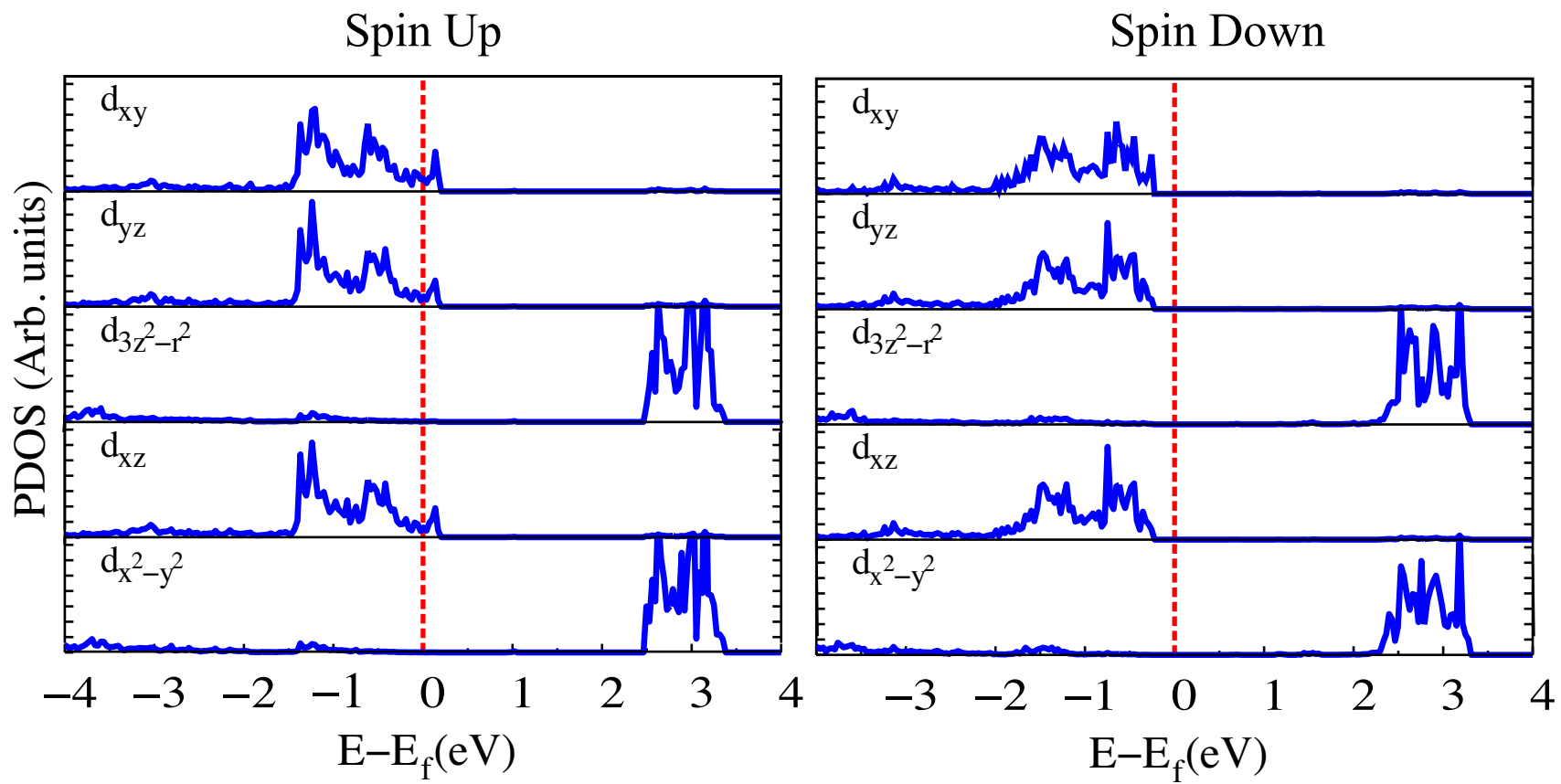


Figure 10 BN11985 26Mar2012

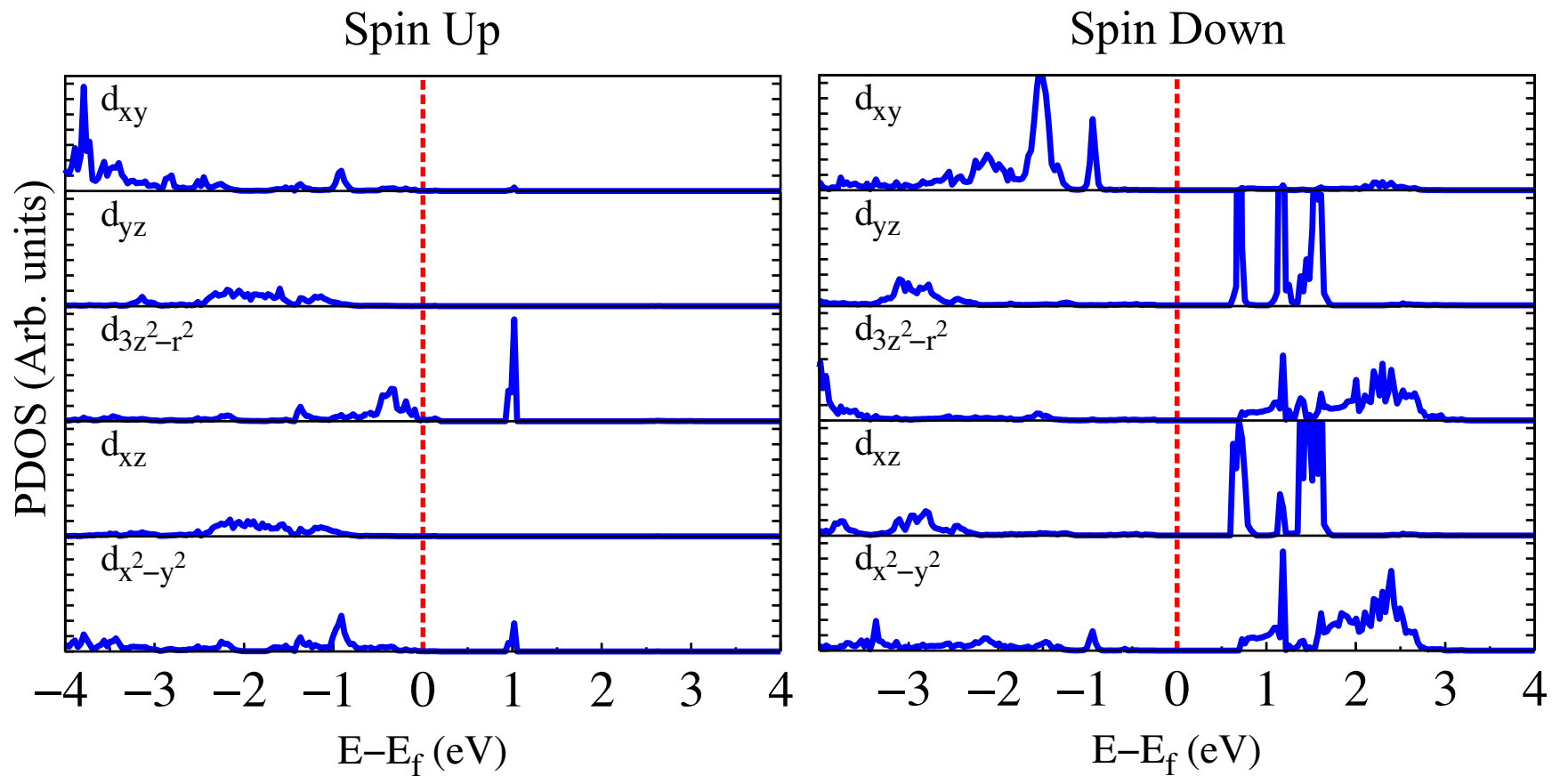


Figure 11 BN11985 26Mar2012

